Doping effects on the structure and electrical properties of $La_2Ce_2O_7$ proton conductors

Javier Zamudio-García[1], Lucía dos Santos-Gómez[1], José Manuel Porras-Vázquez[1], Enrique R. Losilla[1], David Marrero-López[2,*]

[1] *Universidad de Málaga, Dpto. de Química Inorgánica, 29071-Málaga, Spain*

[2] *Universidad de Málaga, Dpto. de Física Aplicada I, 29071-Málaga, Spain*

Keywords: CeO_2; $La_2Ce_2O_7$; structure; proton conductivity

ABSTRACT

Recent studies have reported that the conductivity of $La_2Ce_2O_7$ proton conductors is improved by aliovalent doping, despite the high concentration of oxygen vacancies in the pristine material. In this study, we provide new insights into the structural and conducting properties of $La_{2-x}A_xCe_2O_{7\pm\delta}$ (A= Na^+, Ca^{2+}, Sr^{2+}, Ba^{2+}, Y^{3+} and W^{6+}; $x \leq 0.2$). The materials are apparently single phase compounds by conventional X-ray diffraction with a disordered fluorite-type structure; however, the local structure, studied by Raman spectroscopy, reveals a biphasic mixture of fluorite and C-type phases, which depends on dopant type and the sintering temperature. In addition, phase segregations are observed for Ca, Sr and Ba-doped samples by scanning electron microscopy. The different substitutions do not improve the bulk conduction at low temperature, and the conductivity differences between the samples are mainly ascribed to microstructural changes. High sintering temperatures produce a significant reduction of the bulk conductivity, i.e. 1.38 and 1.01 μS cm^{-1} at 300 ºC for samples sintered at 1400 and 1500 ºC, respectively. The use of Zn as sintering aid greatly improves the densification of $La_2Ce_2O_7$ at lower temperature, without affecting negatively the conductivity.

* Corresponding author.

E-mail address: marrero@uma.es (David Marrero-López)

Present address: Dpto. de Física Aplicada I, Facultad de Ciencias, Campus de Teatinos, Universidad de Málaga, 29071-Málaga, Spain.

Tel: +34 952137057, Fax: +34 952132382

1. Introduction

Ceramic proton conductors are attracting great attention because of their potential applications in energy production and storage, including electrolytes for solid oxide fuel cells, hydrogen separation membranes and gas sensors [1-4]. However, the poor stability of the traditional materials under operating conditions is the main obstacle for their commercialization, and therefore, new stable compounds are needed [5-7].

Most of the research on proton conducting ceramics has been focused on perovskite based materials [8,9]. Among these materials, $BaCeO_3$ has the highest proton conductivity; however, Ce-containing oxides shows poor phase stability in H_2O and CO_2 environments [10-14]. On the contrary, $BaZrO_3$ shows improved carbonation resistance, but requires high sintering temperatures to reach densification and reduce the high grain boundary resistance [14,15]. In this context, a useful strategy to improve the densification of $BaZrO_3$ is the addition of transition metals as sintering aids, such as Zn, which allows a considerable reduction of the sintering temperature [15,16].

Low doped $Ce_{1-x}La_xO_{2-x/2}$ ($x \leq 0.2$) are compounds with fluorite type-structure and good oxide ion conductivity at intermediate temperatures (500-800 ºC) [17-19]. For high La-substitution levels a pyrochlore-type structure ($La_2Ce_2O_7$) is reported, which exhibits proton conductivity in humidified atmosphere below 450 ºC and high CO_2 stability [20,21]. Furthermore, under reducing conditions, this material is a mixed ionic-electronic conductor due to the partial reduction of Ce^{4+} to Ce^{3+} with the consequent formation of electronic charge carriers, making it of interest for hydrogen membrane applications [22,23].

Regarding the real structure of $La_2Ce_2O_7$ (LCO), there exists many controversies from both experimental and theoretical studies. Some authors have reported that LCO crystallizes with a pyrochlore-type structure, while others have suggested a disordered fluorite with composition $Ce_{0.5}La_{0.5}O_{1.75}$ [24-26]. Recently, our research group has studied the local structure of $Ce_{1-x}La_xO_{2-x/2}$ ($x \leq 0.7$) series by transmission electron microscopy (TEM) and μ-Raman spectroscopy [27]. The results revealed a biphasic mixture of disordered fluorite (s.g. $Fm\bar{3}m$) and C-type (s.g. $Ia\bar{3}$) phases for $0.4 \leq x \leq 0.6$, similar to that observed previously for highly Sm- and Gd-doped CeO_2 [28]. In addition, the water uptake and proton conductivity increased gradually with the La-content, indicating that the formation and percolation of the C-type phase are responsible for the proton conduction in these materials. The C-type structure is typical of rare-earth sesquioxides, where the oxygen vacancy ordering leads to a 2×2×2 supercell relative to the ideal cubic fluorite [27-30]. Since the structures of fluorite and C-type phases are similar, the diffraction peaks are overlapped, hindering the structural analysis by conventional diffraction techniques.

In this context, Raman spectroscopy is a more efficient technique than XRD to study the short-range of non-stoichiometric materials [31,32]. This technique is highly sensitive to identify the formation of oxygen vacancies as well as changes in the oxygen atomic positions, and has been widely used to study the local structure of rare-earth doped CeO_2 and differentiate between fluorite and C-type phase formation [27-33].

In order to increase the conductivity of $La_2Ce_2O_7$, which is much lower than that of the traditional $BaCeO_3$, different doping strategies have been explored partially substituting La^{3+} for Na^+, Sr^{2+}, Ca^{2+}, Mg^{2+}, Nd^{3+}, Sm^{3+}, Y^{3+}, In^{3+} and Mo^{6+} [34-40], and Ta^{5+} in the Ce^{4+} site [41]. In most of the cases, the aliovalent doping produces a slight increase of the ionic conductivity, which is attributed to the creation of additional oxygen vacancies in the structure. However, in the case the of trivalent rare-earth dopants, such as Y^{3+}, the increase of conductivity is explained by disordering of the oxygen vacancies, although it has been not confirmed by a structural analysis [42]. Thus, the effects of these dopants on the crystal structure and transport properties of $La_2Ce_2O_7$ remain unclear, because the increase of the oxygen vacancy concentration in highly La-doped CeO_2 is expected to decrease the total conductivity due to the stronger oxygen vacancy-dopant interaction [27].

The aim of this work is to reexamine the effect of different cation substitutions, i.e. Na^+, Ca^{2+}, Sr^{2+}, Ba^{2+}, Y^{3+} and W^{6+} on the crystal structure and transport properties of $La_2Ce_2O_7$. For this purpose, a freeze-drying precursor method is employed to obtain full dense ceramic materials with an optimized microstructure at relatively low sintering temperature. The phase composition and the crystal structure are investigated by X-ray diffraction, μ-Raman spectroscopy and electron microscopy. Finally, the total conductivity is determined by impedance spectroscopy and the results are compared with those previously reported in the literature.

2. Experimental

2.1. Synthesis

Polycrystalline powders of $La_{2-x}A_xCe_2O_{7\pm\delta}$ (A= Na^+, Ca^{2+}, Sr^{2+}, Ba^{2+}, Y^{3+} and W^{6+}, $0 \leq x \leq 0.2$) were prepared from freeze-dried precursors as described in details elsewhere for related materials [27]. Stoichiometric amounts of $Ln(NO_3)_3 \cdot 6H_2O$ (Ln=Ce, La and Y), $A(NO_3)_2$ (A=Ca, Sr and Ba) and Na_2CO_3 were dissolved in water and diluted nitric acid, respectively, while WO_3 was dissolved in a diluted ammonia solution. All the reactants have a purity above 99.9% and were supplied by Sigma-Aldrich. EDTA (Ethylenediaminetetraacetic acid) was added as a complexing agent to stabilize the solutions in a ligand to metal molar ratio of 1:1. The cation solutions, with a concentration and pH of about 0.1 mol L^{-1} and 7, respectively, were frozen in liquid nitrogen and then dehydrated for 2 days in a freeze-dryer (Scanvac-Coolsafe). The precursors were subsequently fired at 300 and 800 ºC for 1 h to achieve crystallization. After that, the polycrystalline powders were compacted into disks of 10 and 1 mm of diameter and thickness, respectively, and sintered at 1400 ºC for 1 h. Furthermore, pellets of $La_2Ce_2O_7$ were also prepared at 1300 and 1500 ºC for 1 h to evaluate the effect of the sintering temperature on the structure and transport properties. The relative density of the pellets was determined from the mass and volume of the samples and by the Archimedes´s method, obtaining reproducible results.

In order to reduce the sintering temperature of the ceramic pellets, Zn was used as sintering additive. For this purpose, the polycrystalline powders calcined at 800 ºC were mixed with 2 wt.% of ZnO from an ethanol

solution of $Zn(NO_3)_2 \cdot 6H_2O$. This amount of the sintering additive was chosen because this is the optimal one used in the literature for related materials, such as $BaCeO_3$ [16,43]. After calcination at 800 ºC to decompose the nitrate into oxides, the powders were compacted into disks and sintered between 1000 and 1100 ºC for 5 h.

All samples were slowly cooled to room temperature at 5 ºC min^{-1} to ensure an oxygen stoichiometry close to the equilibrium. Finally, the pellets were finely ground in an agate mortar for the structural analysis. For simplicity reasons, the samples are hereafter labelled as LCO for the pristine material and A_x for the doped compounds, $La_{2-x}A_xCe_2O_{7\pm\delta}$, where A and x represent the dopant content, respectively (Table 1).

2.2. Characterization

The purity and structure of the materials were studied by X-ray diffraction (XRD) of powder samples with an Empyrean PANalytical diffractometer. The structural analysis was performed using the GSAS and X'Pert HighScore Plus software [44,45]. μ-Raman spectroscopy was performed by means of a JASCO NRS-5100 spectrometer using a laser output of 532 nm of wavelength at 4.6 mW.

The morphology and cation composition of the pellets were studied with a FEI-Helios Nanolab electron microscope, equipped with an X-Max Oxford energy dispersive X-ray spectrometer (EDX). The average grain size of the dense ceramic pellets was estimated from the linear intercept technique.

The total conductivity was determined by impedance spectroscopy with a 1260 Solartron frequency response analyzer. The measurements were performed in the temperature range of 200-800 °C in dry and wet synthetic air (2 vol.% H_2O) with a dwell time of 60 min to ensure thermal stability at each temperature. Prior to the electrical measurements, the pellet surfaces were coated with Pt ink and fired in air at 800 ºC for 1 h to obtain a current collector layer. The spectra were analyzed with Zview software (Scribner Associates).

3. Results and discussion

3.1. Phase composition and average structure

XRD patterns of $La_{1.9}A_{0.1}Ce_2O_{7\pm\delta}$ (A=Ca^{2+}, Na^{+}, Y^{3+} and W^{6+}) materials suggest that apparently single phase compounds are obtained, without additional diffraction peaks attributed to secondary phases (Fig. 1a). The average structure can be considered as a disordered fluorite (s.g. $Fm\bar{3}m$) because no reflections attributed to the pyrochlore or C-type structures, with oxygen vacancy ordering, are observed. It is also remarkable to comment that it is not possible to distinguish between a mixture of fluorite and C-type phases by conventional diffraction techniques due to the similarity of both structures as aforementioned [27].

The results of the structural analysis in the $Fm\bar{3}m$ s.g. are given in Table 1 and representative examples of the Rietveld refinements are shown in Fig. 2. In the case of the Ba-doped samples, pure compounds are not obtained, $Ba_{0.1}$ contains a 4 wt.% of $Ba(Ce,La)O_3$ (Fig 2b). The disagreement factors are similar for the different samples, taking values of R_F =1.1 - 3.0% and R_{wp}=5.8 - 8.9%, and confirming no significant structural differences between the materials.

Samples with different Sr-content, $0.05 \leq x \leq 0.15$, are also apparently pure compounds by XRD (Fig. 1b); nevertheless, the unit cell volume clearly decreases with the Sr-content, contrary to the expected trend because the ionic radii of La^{3+} (1.16 Å) is smaller than that of Sr^{2+} (1.26 Å) in eightfold coordination (Table 1). In contrast, Y and W -doping leads to a reduction of the cell volume due to the smaller ionic radii of Y^{3+} (1.019 Å) and W^{6+} (0.83 Å) compared to La^{3+} (1.16 Å).

On the other hand, Zn-addition does not produce any detectable secondary phase by XRD, suggesting that this is highly dispersed at the grain boundary region or present as a low crystalline phase (Fig. 1c).

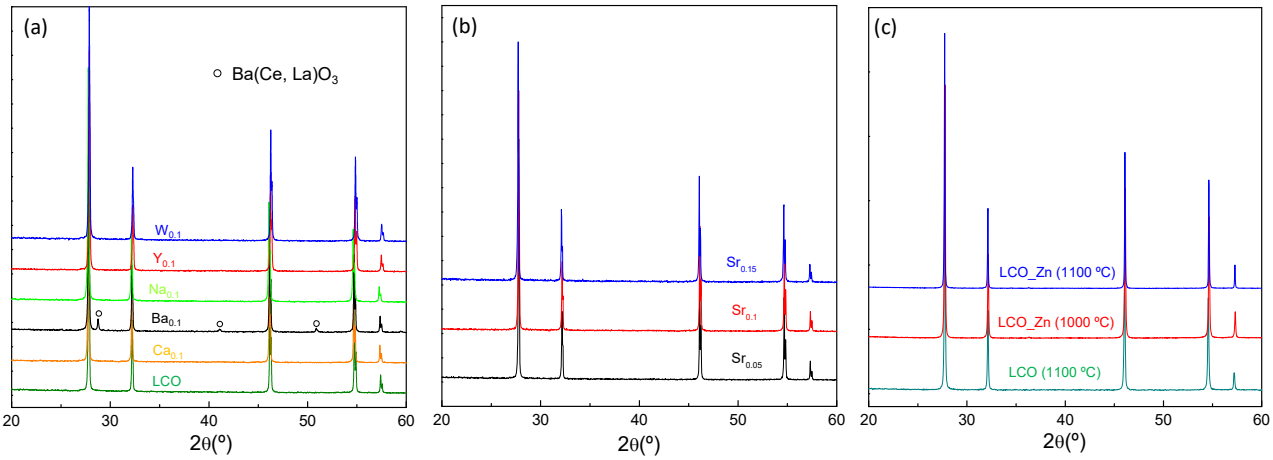

Fig. 1. X-ray diffraction patterns of (a) doped $La_{1.9}A_{0.1}Ce_2O_{7\pm\delta}$ (A= Na^+, Ca^{2+}, Ba^{2+}, Y^{3+} and W^{6+}), (b) $La_{2-x}Sr_xCe_2O_{7-\delta}$ (x=0.05, 0.1 and 0.15), (c) $La_2Ce_2O_7$ with Zn addition and sintered at 1000 and 1100 ºC for 5 h.

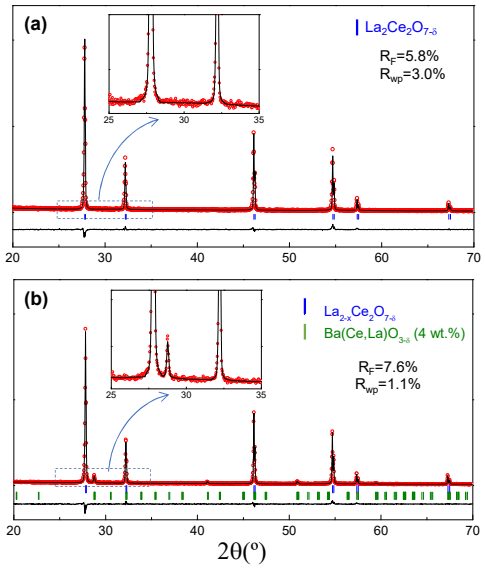

Fig. 2. Selected region of the Rietveld plots of (a) $La_2Ce_2O_7$ and (b) $La_{1.9}Ba_{0.1}Ce_2O_{7\pm\delta}$ by considering a disordered fluorite structure (s.g. $Fm\bar{3}m$).

Table 1. Composition and properties of the materials studied in the present work: unit cell volume, relative density (ρ), average grain size of the pellets (D), bulk conductivity in wet/dry air at 300 ºC, total conductivity in wet air at 700 ºC and activation energy of the total conductivity.

Sample	Abbreviation	V/Z (Å^3)	R_{wp} / R_F (%)	ρ (%)	D (µm)	σ_{bulk}^{wet} (µS·cm^{-1})	σ_{bulk}^{dry} (µS·cm^{-1})	σ_{total} (mS·cm^{-1})	E_a (eV)
1300 ºC	LCO_1300	43.15(2)	6.2/2.1	90	0.6	-	-	--	--
$La_2Ce_2O_7$ 1400ºC	LCO_1400	43.16(2)	5.8/3.0	98	2.5	2.53	1.38	7.3	0.95
1500 ºC	LCO_1500	43.17(2)	6.5/2.9	100	8.5	2.04	1.01	7.8	0.98
$La_{1.9}Na_{0.1}Ce_2O_7$ 1500ºC	$Na_{0.1}$	43.14(2)	7.9/1.9	98	3.3	2.71	-	8.9	0.9
$La_{1.9}Ca_{0.1}Ce_2O_7$	$Ca_{0.1}$	43.00(2)	7.8/2.0	99	4.5	1.50	-	5.4	0.99
$La_{1.95}Sr_{0.05}Ce_2O_7$	$Sr_{0.05}$	43.16(2)	8.2/1.8	98	5.1	2.18	0.81	6.7	0.96
$La_{1.9}Sr_{0.1}Ce_2O_7$	$Sr_{0.1}$	43.15(2)	7.5/1.9	98	9.4	1.80	0.80	5.8	0.97
$La_{1.9}Sr_{0.15}Ce_2O_7$	$Sr_{0.15}$	43.14(2)	7.9/2.5	98	16.4	1.87	0.98	6.1	0.98
$La_{1.9}Ba_{0.1}Ce_2O_7$	$Ba_{0.1}$	43.17(2)	7.6/1.1	99	2.0	3.58	-	8.5	0.92
$La_{1.9}Y_{0.1}Ce_2O_7$	$Y_{0.1}$	42.95(2)	7.6/2.3	100	1.6	2.06	-	7.4	0.99
$La_{1.8}Y_{0.2}Ce_2O_7$	$Y_{0.2}$	42.74(2)	8.9/2.5	99	1.5	1.64	-	6.7	1.00
$La_{1.9}W_{0.1}Ce_2O_7$	$W_{0.1}$	42.80(2)	8.9/1.4	98	1.1	2.76	1.29	6.3	0.93
$La_2Ce_2O_7$-Zn	LCO_Zn	43.18(2)	6.59/2.1	97	0.7	2.45	1.25	6.5	0.93

3.2. μ-Raman

Figure 3a compares the spectra of samples with the same dopant content x=0.1. Undoped CeO_2, included for comparison purposes, shows only a sharp and symmetric band at 465 cm^{-1} corresponding to the F_{2g} mode of the Ce-O bond in an eightfold coordination [32]. The form of this band suggest that CeO_2 is an ordered system with the contribution of phonons only from the center of the Brillouin zone [46]. The introduction of dopants leads to the apparition of new asymmetric and broadening bands. The F_{2g} signal becomes broader for $La_2Ce_2O_7$ as a consequence of the loss of translational symmetry with the introduction of anion defects in the fluorite lattice.

All doped samples show a band centered at ~550 cm^{-1}, which is associated with the formation of oxygen vacancies and their interaction with the six nearest neighbor oxygens (V-O) [47]. It is obvious that the relative intensity of this band depends on the dopant-type and content. This is more intense for $Sr_{0.1}$, confirming that a fraction of Sr^{2+} is incorporated into the lattice, resulting in higher oxygen vacancy concentration. Isovalent Y^{3+}-doping does not modify the oxygen vacancy concentration and the intensity of this band remains unchanged. A similar behavior is observed for Na^{+}-doping, although a significant increase of the oxygen vacancy content is expected. Finally, high valence W^{6+}-doping in the La^{3+} site reduces the concentration of oxygen vacancies, and consequently, the intensity of this band decreases.

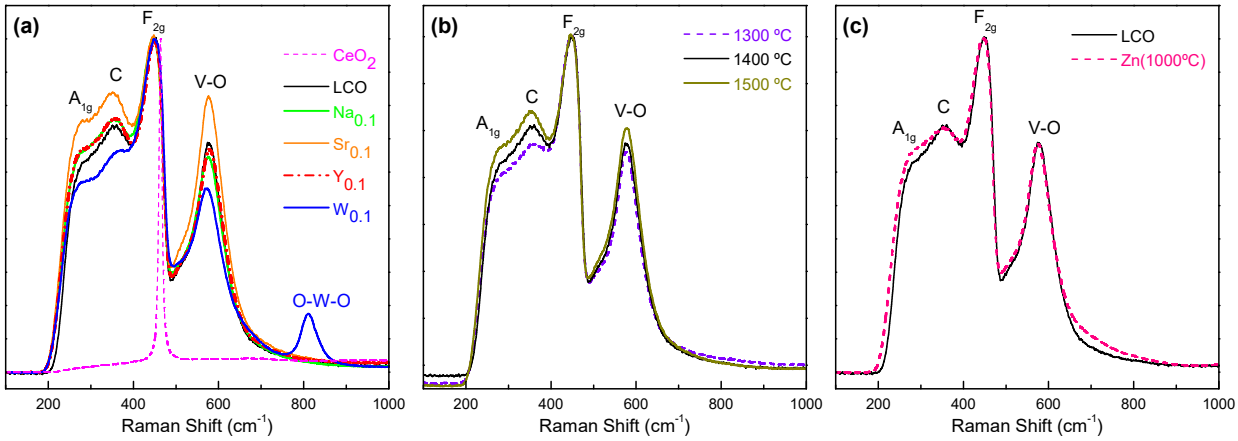

Fig. 3. μ-Raman spectra of (a) undoped and doped $La_{1.9}A_{0.1}Ce_2O_{7\pm\delta}$ (A= Na^{+}, Sr^{2+}, Y^{3+} and W^{6+}), (b) $La_2Ce_2O_7$ sintered between 1300 and 1500 ºC for 1 h, and (c) $La_2Ce_2O_{7-\delta}$ with Zn additive. The spectra of CeO_2 is included for comparison purpose in (a). All the spectra are normalized by the intensity of the F_{2g} band.

The band at 350 cm^{-1} is assigned to the C-type structure, produced by the symmetrical stretching vibrational mode of Ce-O in a sixfold coordination, in accordance with previous studies [32,33]. On the other hand, the band located at 260 cm^{-1} (A_{1g}) is similar to that observed by Nakajima *et al.* in Y-doped CeO_2, which is also attributed to the formation of the oxygen vacancies [48]. It is worth noting that the intensity of the A_{1g}, V-O and C bands follow the same trend, either increasing or decreasing after doping, and evidencing a clear relationship between the

stabilization of the C-type phase and the high concentration of oxygen vacancies in the lattice. In particular, Sr-doping increases both the oxygen vacancy concentration and the amount of C-type phase. In contrast, W-doping leads to a decrease of the oxygen vacancy concentration as well as the amount of C-type phase. This last compound shows and additional band at 810 cm^{-1}, similar to that of fluorite related La_6WO_{12}, corresponding to the stretching vibration of O-W-O groups [49].

The increase of the sintering temperature leads to gradual increase of the C-band, indicating a higher stabilization of the C-type phase (Fig. 3b). In the case of the samples with Zn-addition, the spectra are similar to that of LCO, suggesting that Zn does not modify substantially the structure and the oxygen sublattice, in accordance with the XRD results (Fig. 3c). All these results further evidence the presence of a biphasic mixture of fluorite and C-type phases, contrary to the results reported into the literature for related materials, where a disordered fluorite is considered [34-41].

3.3. Microstructure and elemental composition

SEM images for pellets with different Sr-content are shown in Fig. 4. All of them present high densification with relative densities above 98% after sintering at 1400 ºC for 1 h. The main differences between the samples is the average grain size, which grows significantly with increasing Sr-content from 2.5 µm for LCO to 16.4 µm for $Sr_{0.15}$. In addition, nanometric particles are observed at the grain boundary region and on the pellet surface, where large aggregates are eventually formed for highly doped samples. EDX analysis confirms that these particles are rich in Sr and therefore are assigned to SrO and $SrCO_3$ segregations (Fig. 5a). In addition, the composition of the grain interior reveals that only 55 wt. % of Sr is incorporated into the structure. Thus, the solubility limit of Sr in $La_{2-x}Sr_xCe_2O_{7-x/2}$ is $x \leq 0.05$, the excess of Sr is segregated in the form of low crystalline $SrCO_3$ particles. These findings explain why secondary phases are not detected by XRD analysis as well as the anomalous variation of the unit cell volume, decreasing with the increasing Sr-content, contrary to the expected behavior, as aforementioned.

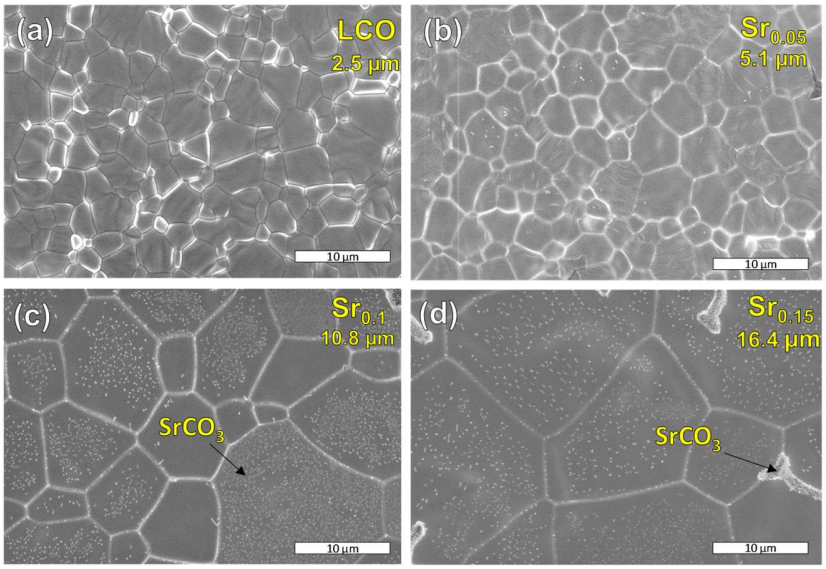

Fig. 4. SEM image of $La_{2-x}Sr_xCe_2O_{7-\delta}$ pellets sintered at 1400 ºC for 1 h with different Sr-content (a) x=0, (b) x=0.05, (c) x=0.1 and (d) x=0.15. Small particles of $SrCO_3$ are observed on the surface and at the grain-boundary region of the pellets.

On the other hand, the Sr-enrichment at the grain boundary produces a significant grain growth, possibly associated with the formation of a liquid phase, which enhances the grain boundary diffusion during the sintering process. The amount of Sr-segregation for $x \leq 0.1$ is sufficiently low and disperse to avoid the mechanical failure of the samples due to carbonation. Similarly, Ca-doped samples show phase segregations of $CaCO_3$, which are also undetectable by XRD (Fig. 5b). In Ba-doped samples, small grains of $Ba(Ce,La)O_{3-\delta}$ are identifiable, and the composition of the grain interior reveals a negligible Ba-content, within the experimental error of the technique, indicating that Ba solubility in $La_2Ce_2O_7$ is relatively low (Fig. 5c). Y and W-doped samples do not show appreciable phase segregations and the grain size is somewhat lower than that of LCO (Table 1). Na-doped samples, sintered at 1400 ºC, are porous (Fig. 5e) and therefore, they are sintered at 1500 ºC for 5 h to increase the relative density up to 98%, comparable to the other samples.

LCO pellets with 2 wt.% of Zn exhibit relative density above 97% after sintering at 1000 ºC, thus the densification temperature is reduced 400 ºC compared to the same samples without sintering aids (Fig. 6). The grain size is also substantially reduced to 0.7 µm (Table 1). Moreover, phase segregations are not detected by EDX.

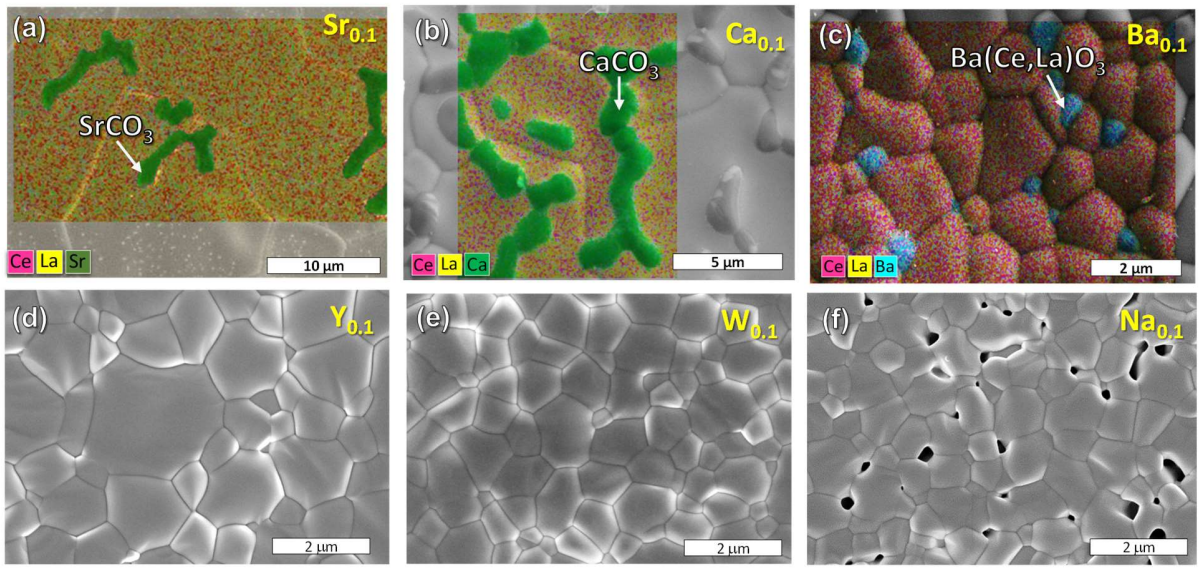

Fig. 5. SEM and EDX image of the sintered pellets of $La_{1.9}A_{0.1}Ce_2O_{7-\delta}$ at 1400 ºC for 1 h, A= (a) Sr (b) Ca, (c) Ba, (d) Y, (e) W and (f) Na. Secondary phases are detected by EDX analysis for Ca, Sr and Ba-doping.

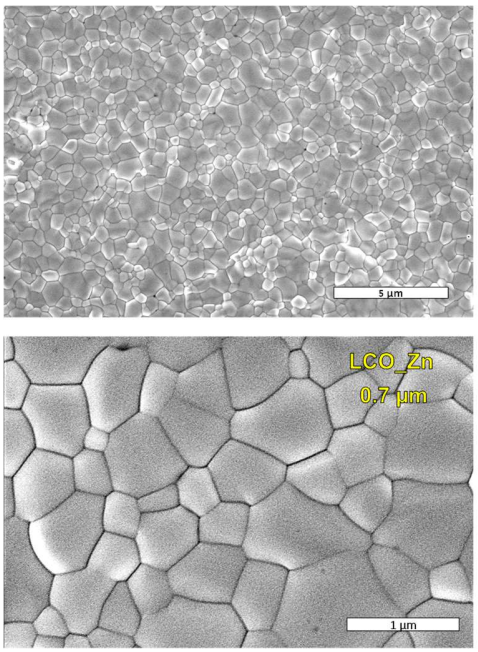

Fig. 6. SEM image at different magnification of $La_2Ce_2O_{7-\delta}$ pellets with Zn addition and sintered at 1000 ºC for 5 h.

3.4. Conductivity

The impedance spectra show three different processes assigned to the bulk and grain-boundary conduction in the electrolyte, and the electrode response at low frequency (Fig. 7). The data are adequately fitted by a simple equivalent circuit consisting of serial (RQ) elements, where R is a resistance in parallel with Q a constant phase element (inset Fig. 7b). For all the pellets, the grain boundary response is only observable at temperatures lower than 350 ºC, indicating that the bulk conduction is the main contribution to the total conductivity. Even samples containing secondary phases, i.e. Ca, Sr and Ba, exhibit relatively low grain-boundary resistance, which is mainly attributed to the large grain size of the pellets and the lower number of grain boundaries. The bulk contribution exhibits typical capacitance values of 5 pF cm^{-1}, regardless the composition of the samples, while the grain boundary contribution has a capacitance of 2 nF cm^{-1} [50].

The impedance spectra of LCO in dry and wet air (2 vol.% H_2O) confirm the presence of a significant proton conductivity at low temperature (Fig. 7a). In addition, the increase of the sintering temperature produces a significant increase of the bulk resistance, possibly attributed to different amount of C-type phase with lower conductivity, as confirmed by Raman analysis. Indeed, the wet to dry conductivity ratio increases from 1.8 to 2.0 for samples prepared at 1400 and 1500 ºC, respectively, suggesting a higher content of C-type phase with proton conductivity.

In general, the introduction of dopants into $La_2Ce_2O_7$ leads to a decrease of the bulk conductivity at low temperature. Fig. 7b clearly indicates that the bulk resistance increases with increasing Y-doping, which is explained by the lower ionic radii of Y^{3+}(1.019 Å) in relation to La^{3+}(1.16 Å). This produces a shrinkage of the unit cell, limiting the free space for proton mobility, and consequently, the conductivity decreases. In contrast, a previous study suggested that the ionic conductivity of Y-doped $La_2Ce_2O_7$ increases because the introduction of Y in the structure produces a disordered of the oxygen sublattice, improving the oxygen vacancy mobility, although this is not confirmed by a structural analysis [42]. It is worth noting that a disordering of the oxygen sublattice is expected to decrease the fraction of C-type phase. However, the Raman spectra indicates that LCO and $Y_{0.1}$ samples exhibit the same local structure with similar fraction of fluorite and C-type phases. Hence, the improvement of conductivity observed previously by Zhang *et al*. is possibly attributed to microstructural changes as described below [42].

Samples with Zn exhibit bulk conductivity comparable to the pristine material, confirming that the transport properties of LCO are not seriously affected by the use of sintering aids (Fig. 7c). Only a slight increase of the grain-boundary resistance is observed, which is attributed to the smaller grain size.

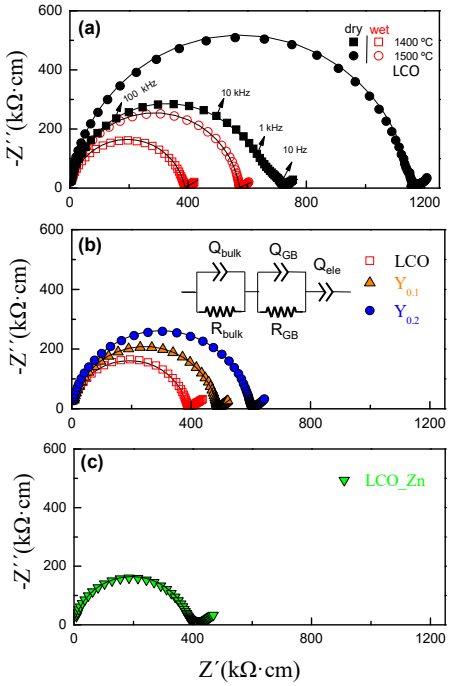

Fig. 7. Nyquist plots at 300 ºC for (a) $La_2Ce_2O_7$ sintered at 1400 and 1500 ºC for 1 h in dry and wet air, (b) Y-doped $La_2Ce_2O_7$ in wet air, and (c) $La_2Ce_2O_7$ with Zn addition in wet air. The equivalent circuit model used to fit the data is given in the inset of (b).

The Arrhenius plots of total conductivity are shown in Fig. 8. The conductivity of the Sr-doped samples decreases nearly linearly with the Sr-content from 7.3 mS cm^{-1} for LCO to 6.1 mS cm^{-1} for $Sr_{0.15}$ at 700 ºC, which is explained by a higher amount of C-type phase with lower conductivity (Fig. 8a). A similar trend is observed for the Y-doped samples, in this case the oxygen vacancy content does not vary, and therefore, the lower conductivity is attributed to the smaller unit cell volume, limiting the ionic mobility (Fig. 8b). The lowest values of conductivity are found for Ca- and W-doping due to the different cation size mismatch at the La-site, which produces a large distortion of the unit cell volume and therefore lowers the ionic mobility.

In the case of Ba-doped samples, the values of conductivity are somewhat higher than those of LCO, i.e. 8.5 mS cm^{-1} at 700 ºC. By considering that the Ba incorporation in the structure is negligible, the improvement of conductivity is explained by the segregation of $Ba(Ce,La)O_{3-\delta}$ with higher proton conductivity than that of $La_2Ce_2O_7$. It is also worth noting that $BaCe_{1-x}La_xO_{3-\delta}$ and $Ce_{1-x}La_xO_{2-\delta}$ have similar thermal expansion coefficients, about $11.2 \cdot 10^{-6}$ and $12.3 \cdot 10^{-6}$ K^{-1}, respectively, and therefore, they are mechanically compatible [51,52]. Thus, the preparation of composite grade membranes of both materials could be of interest for hydrogen membrane applications by combining their properties: the better phase stability of $Ce_{1-x}La_xO_{2-\delta}$ in CO_2 and H_2O environments and the higher proton conductivity of $BaCe_{1-x}La_xO_{3-\delta}$.

Na-doped sample shows an unusual increase of the conductivity, especially at high temperature with a value of 8.9 mS cm^{-1} at 700 ºC, which is higher than that reported by Tu *et al.*, i.e. 7.0 mS cm^{-1} [29] (Fig. 8c). However, XRD data and Raman spectra reveal that the local structure is not affected by Na-doping, suggesting that the improvement of conductivity is possibly associated with the higher sintering temperature (1500 ºC) needed to reach densification. Na^{+} segregation at the grain boundary region could also improve the total conductivity at high temperature, as observed previously in Y-doped ZrO_2 [53].

Samples with Zn exhibit slightly lower conductivity than that of the pristine compound, i.e. 7.3 and 6.5 mS cm^{-1} and for LCO and Zn-containing samples, respectively, at 700 ºC (Fig. 8d). This reduction of the conductivity is attributed to the lower grain size of the pellets and possibly minor incorporation of the transition metals into the fluorite lattice. Similar findings are observed in $BaCeO_3$-based electrolytes with transition metals as sintering aids [43].

Regarding the values of activation energy of the total conductivity, these varies between 0.92 and 1.0 eV. The activation energy for the parent compound increases with the sintering temperature from 0.95 to 1.0 eV at 1400 and 1500 ºC, respectively, in accordance with the increase of bulk conductivity at low temperature. In general, the introduction of dopants leads to an increase of the activation energy, e.g. 0.96, 0.97 and 0.98 eV for $Sr_{0.05}$, $Sr_{0.1}$ and $Sr_{0.15}$, respectively, attributed to a reduction of the unit cell volume, limiting the free space for the ionic conduction. A similar trend is observed for Y-doped samples. The lowest activation energy ~0.92 eV is observed for $Ba_{0.1}$, which can be explained by larger unit cell volume of this phase, and the presence of a significant amount of high conducting $Ba(Ce,La)O_3$ phase. It is also worth noting that the values of activation obtained herein are somewhat lower than those previously reported (Table 2).

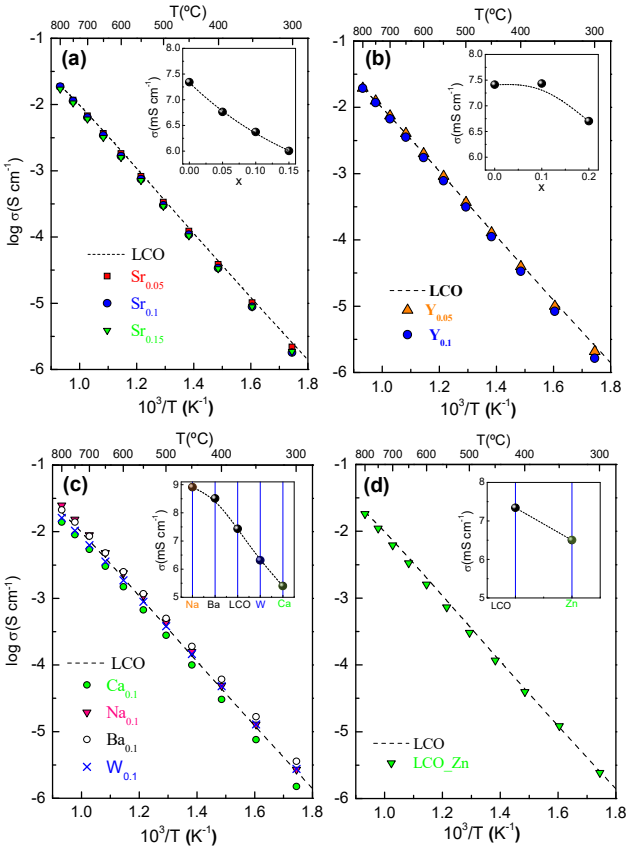

Fig. 8. Arrhenius plots of the total conductivity of (a) Sr-doped $La_2Ce_2O_7$, (b) Y-doped $La_2Ce_2O_7$, (c) $La_{1.9}M_{0.1}Ce_2O_{7\pm\delta}$ (M= Na, Ca, Ba and W), (d) samples with Co and Zn addition as sintering aids. The insets show the variation of the conductivity with the dopant type or content at 700 ºC.

Table 2 compares the values of total conductivity reported in the literature for undoped and doped $La_2Ce_2O_7$. The conductivity of the pristine material varies from 4.0 to 7.3 mS cm^{-1} at 700 ºC, depending on the sintering temperature. In particular, the total conductivity in the high temperature range increases slightly with the sintering temperature, although the bulk conductivity at low temperature decreases, i.e. 7.3 and 7.8 mS cm^{-1} for samples prepared at 1400 and 1500 ºC, respectively. Similarly, Tu *et al.* reported a conductivity of 4.8 mS cm^{-1} for samples sintered at 1500 ºC for 5 h, while, Yamamura *et al.* obtained a value of 7.1 mS cm^{-1} for pellets sintered at 1600 ºC for 10 h [54]. These differences could be explained by the different sintering temperature and the resulting microstructure of the samples, i.e. relative density and grain size. Bearing in mind that these materials are a biphasic mixture of fluorite and C-type phases, the preparation conditions, sintering temperature and the cooling rate, may affect the oxygen ordering, and consequently, the amount of stabilized C-type phase with lower ionic conductivity. In addition, high sintering temperature alters the cation stoichiometry of the materials due to possible cation evaporation losses and the formation of minor phase segregations as observed in doped $BaCeO_3$ [55].

Table 2. Conductivity at 700 ºC and activation energy of $La_2Ce_2O_7$–based materials reported in the literature.

Composition	σ_t(mS cm^{-1})	E_a(eV)	Sintering	ρ(%)	Ref.
$La_2Ce_2O_7$	7.3	0.95	1400 / 1h	98	This work
$La_2Ce_2O_7$	7.8	1.0	1500 / 1h	100	This work
$La_2Ce_2O_7$	7.1	1.03	1600ºC / 10h	95	[54]
$La_2Ce_2O_7$	4.0	--	1500ºC /6h	94	[21]
$La_2Ce_2O_7$ $La_{1.9}Na_{0.1}Ce_2O_7$	4.8 7.0	--	1500 / 5h	-	[36]
$La_2Ce_2O_7$ $La_{1.9}Mo_{0.1}Ce_2O_7$	5.5 7.4	1.12 0.99	1500 / 5h	-	[40]
$La_2Ce_2O_7$ $La_{1.9}Y_{0.1}Ce_2O_7$ $La_{1.9}In_{0.1}Ce_2O_7$	5.5 6.8 8.2	1.12 1.12 1.04	1500 / 5h	96 96 99	[42]

In the $Ce_{1-x}La_xO_{2-\delta}$ series, the conductivity decreases monotonously with the increase of La-content due to high oxygen vacancy concentration and their interaction with the dopant ions, therefore, the conductivity of $La_2Ce_2O_7$ is not expected to increase with aliovalent dopant [27]. In the present study, most of the aliovalent dopant decreases the total conductivity of $La_2Ce_2O_7$; however, several authors have reported slightly higher values of conductivity for doped $La_2Ce_2O_7$ (Table 2). For instance, Tu *et al.* reported a conductivity of 4.8 and 7.0 mS cm^{-1} for LCO and $Na_{0.1}$ at 700 ºC, respectively [36]. The same authors reported a conductivity of 5.5 and 8.2 mS cm^{-1} for LCO and $In_{0.1}$ at 700 ºC, respectively; however, it is important to notice that In-doped samples exhibit higher relative density and larger grain size compared to the pristine material. Particularly, indium is widely used to enhance the densification of proton conductors, such as $BaZrO_3$ [56]. A similar behavior is observed for Gd-doped CeO_2 with Na-addition [57].

In summary, the conductivity differences, reported in the literature between undoped and doped $La_2Ce_2O_7$, are relatively small to be attributed to an improvement of the intrinsic bulk conduction. Indeed, the conductivity depends on the synthesis method and thermal treatment. Thus, the main effect of the dopant in LCO is to modify the microstructure rather than the intrinsic bulk conductivity. Further investigations are need to explain in details these relations, including a structural analysis at high temperature and the determination of the ionic and electronic contributions to the total conductivity.

4. Conclusions

A freeze-drying precursor method was used to obtain full dense ceramic pellets of $La_{2-x}A_xCe_2O_{7\pm\delta}$ (A= Ca^{2+}, Sr^{2+}, Ba^{2+}, Y^{3+}, Na^{+} and W^{6+}; $x \leq 0.2$) proton conductors. The high densification of the samples allowed a straight comparison between the conducting properties. A carefully inspection of the sample by SEM showed that the solubility of Ca, Sr and Ba into $La_2Ce_2O_7$ is relatively low and the excess of dopant is segregated in form of low crystalline phases. The μ-Raman spectra revealed a complex structure, consisting in a biphasic mixture of fluorite and C-type phases. The oxygen vacancy concentration and amount of C-type phase depend on the doping and the thermal treatment of the samples. The bulk conductivity of $La_2Ce_2O_7$ at low temperature decreases with increasing sintering temperature; however, the total conductivity at high temperature increases slightly. In general, the introduction of dopants into $La_2Ce_2O_7$ do not improve the bulk conductivity, contrary to previous studies. The total conductivity variations are more likely to arise from microstructural changes, such as relative density, grain size and grain boundary segregation (e.g. Na^{+}). Finally, the addition of Zn is beneficial to decrease the sintering temperature, without altering significantly the conductivity.

Acknowledgements

This work was supported by MINECO through the RTI2018-093735-B-I00 and MAT2016-77648-R research grants (Spain), which is co-funded by FEDER. J.Z-G thanks to the Spanish Ministry of Education, Culture and Sport for her FPU grant (FPU17/02621). J.M.P-V. thanks the University of Málaga for the funding.

References

(1) Z. Tao, L. Yan, J. Qiao, B. Wang, L. Zhang, J. Zhang, A review of advanced proton-conducting materials for hydrogen separation. Prog. Mater. Sci. 74 (2015) 1–50.

(2) W. Wang, D. Medvedev, Z. Shao, Gas Humidification Impact on the Properties and Performance of Perovskite-Type Functional Materials in Proton-Conducting Solid Oxide Cells. Adv. Funct. Mater. 28 (2018) 1802592.

(3) S. Hossain, A.M. Abdalla, S.N.B. Jamain, J.H. Zaini, A.K. Azad, A review on proton conducting electrolytes for clean energy and intermediate temperature-solid oxide fuel cells. Renew. Sust. Energ. Rev. 79 (2017) 750-764.

(4) N. Kochetova, I. Animitsa, D. Medvedev, A. Demin, P. Tsiakaras, Recent activity in the development of proton-conducting oxides for high-temperature applications. RSC Adv. 6 (2016) 73222-73268.

(5) P. Colomban, Proton conductors and their applications: A tentative historical overview of the early researches. Solid State Ionics 334, (2019), 125-144.

(6) S. Upasen, P. Batocchi, F. Mauvy, A. Slodczyk, P. Colomban. Chemical and structural stability of $La_{0.6}Sr_{0.4}Co_{0.2}Fe_{0.8}O_{3-\delta}$ ceramic vs. medium/high water vapor pressure, Ceramics International, 41 (2015) 14137-14147.

(7) S. Upasen, P. Batocchi, F. Mauvy, A. Slodczyk, P. Colomban, Protonation and structural/chemical stability of $Ln_2NiO_{4+\delta}$ ceramics vs. H_2O/CO_2: High temperature/water pressure ageing tests, J. Alloy. Compd. 622 (2015) 1074-1085.

(8) D. Medvedev, A. Murashkina, E. Pikalova, A. Demin, A. Podias, P. Tsiakaras, $BaCeO_3$: Materials development, properties and application. Prog. Mater. Sci. 60 (2014) 72-129.

(9) H. Dai, H. Kou, H. Wang, L. Bi, Electrochemical performance of protonic ceramic fuel cells with stable $BaZrO_3$ -based electrolyte: A mini-review. Electrochem. Commun. 96 (2018) 11-15.

(10) A. Slodczyk, M. D. Sharp, S. Upasen, P. Colomban, John A. Kilner, Combined bulk and surface analysis of the $BaCe_{0.5}Zr_{0.3}Y_{0.16}Zn_{0.04}O_{3-\delta}$ (BCZYZ) ceramic proton-conducting electrolyte, Solid State Ionics 262 (2014) 870.

(11) T. Somekawa, Y. Matsuzaki, M. Sugahara, Y. Tachikawa, H. Matsumoto, S. Taniguchi, K. Sasaki, Physicochemical properties of $Ba(Zr,Ce)O_{3-\delta}$ -based proton-conducting electrolytes for solid oxide fuel cells in terms of chemical stability and electrochemical performance. Int. J. Hydrog. Energy 42 (2017) 16722-16730.

(12) R.H. Ryu, S.M. Haile. Chemical stability and proton conductivity of doped $BaCeO_3$-$BaZrO_3$ solid solutions. Solid State Ionics 125 (1999) 355-367.

(13) S. V. Bhide, A. V. Virkar, Stability of $BaCeO_3$-based proton conductors in water-containing atmospheres. J. Electrochem. Soc. 146 (1999) 2038-2044.

(14) K. Katahira, Y. Kohchi, T. Shimura, H. Iwahara, Protonic conduction in Zr-substituted $BaCeO_3$, Solid State Ionics 138 (2000) 91-98.

(15) S. Tao, J.T.S Irvine, Conductivity studies of dense yttrium-doped $BaZrO_3$ sintered at 1325 °C. J. Solid State Chem. 180 (2007) 3493-3503.

(16) M. Amsif, D. Marrero-López, J.C. Ruíz-Morales, S.N. Savvin, P. Núñez, The effect of Zn addition on the structure and transport properties of $BaCe_{0.9-x}Zr_xY_{0.1}O_{3-\delta}$. J. Eur. Ceram. Soc. 34 (2014) 1553–1562.

(17) H. Tinwala, P. Shah, K. Siddhapara, D. Shah, J. Menghani, Investigation of ionic conductivity of lanthanum cerium oxide nano crystalline powder synthesized by co precipitation method. J. Cryst. Growth 452 (2016) 54-56.

(18) E. Suda, B. Pacaud, M. Mori, Sintering characteristics, electrical conductivity and thermal properties of La-doped ceria powders. J. Alloy. Compd. 408-412 (2006) 1161-1164.

(19) K. Sandhya, N.S. ChitraPriya, P.K. Aswathy, D.N. Rajendran, Electrical properties of rare earth doped ceria electrolyte for solid oxide fuel cell applications. Materials Today: Proceedings, 10 (2019) 112-120.

(20) W. Sun, S. Fang, L. Yan, W. Liu, Investigation on proton conductivity of $La_2Ce_2O_7$ in wet atmosphere: dependence on water vapour partial pressure. Fuel Cells 12 (2012) 457-463.

(21) V. Besikiotis, C.S. Knee, I. Ahmed, R. Haugsrud, T. Norby, Crystal structure, hydration and ionic conductivity of the inherently oxygen-deficient $La_2Ce_2O_7$. Solid State Ionics 228 (2012) 1-7.

(22) C. Pizzolitto, F. Menegazzo, E. Ghedini, G. Innocenti, A. Di Michele, G. Cruciani, F. Cavani, M. Signoretto, Increase of Ceria Redox Ability by Lanthanum Addition on Ni Based Catalysts for Hydrogen Production. ACS Sustain. Chem. Eng. 6 (2018) 13867-13876.

(23) A.K. Lucid, P.R.L. Keating, J.P. Allen, G.W. Watson, Structure and Reducibility of CeO_2 Doped with Trivalent Cations. J. Phys. Chem. C 120 (2016) 23430-23440.

(24) D.E.P. Vanpoucke, P. Bultinck, S. Cottenier, V. Van Speybroeck, I. Van Driessche, Density functional theory study of $La_2Ce_2O_7$: disordered fluorite versus pyrochlore structure. Phys. Rev. B 84 (2011) 054110.

(25) Q. Zhang, X. Zheng, J. Jiang, W. Liu, Structural stability of $La_2Ce_2O_7$ as a proton conductor: a first-principles study. J. Phys. Chem. C 117 (2013) 20379-20386.

(26) E. Reynolds, P.E.R. Blanchard, Q. Zhou, B.J. Kennedy, Z. Zhang, L.J. Jang, Structural and spectroscopic studies of $La_2Ce_2O_7$: disordered fluorite versus pyrochlore structure. Phys. Rev. B 85 (2012) 132101.

(27) J. Zamudio-García, J.M. Porras-Vázquez, J. Canales-Vázquez, A. Cabeza, E.R. Losilla, D. Marrero-López, Relationship between the Structure and Transport Properties in the $Ce_{1-x}La_xO_{2-x/2}$System. Inorg. Chem. 58 (2019) 9368-9377.

(28) C. Artini, M. Pani, M.M. Carnasciali, M.T. Buscaglia, J.R. Plaisier, G.A. Costa, Structural Features of Sm- and Gd-Doped Ceria Studied by Synchrotron X-ray Diffraction and μ-Raman Spectroscopy. Inorg. Chem. 54 (2015) 4126-4137.

(29) S. Hull, S.T. Norberg, I. Ahmed, S.G. Eriksson, D. Marrocchelli, P.A. Madden, Oxygen vacancy ordering within anion-deficient Ceria. J. Solid State Chem. 182 (2009) 2815-2821.

(30) M. Coduri, M. Scavini, M. Allieta, M. Brunelli, C. Ferrero, Defect Structure of Y-Doped Ceria on Different Length Scales. Chem. Mater. 25 (2013) 4278–4289.

(31) S. Karlin, P. Colomban, Phase Diagram, Short-Range Structure, and Amorphous Phases in the ZrO_2–GeO_2(–H_2O) System, J. Am. Ceram. Soc. 8 (1999) 735-741.

(32) J.R. McBride, K.C. Hass, B.D. Poindexter, W.H. Weber, Raman and x-ray studies of $Ce_{1-x}RE_xO_{2-y}$, where RE=La, Pr, Nd, Eu, Gd, and Tb. J. Appl. Phys. 76 (1994) 2435-2441.

(33) S. Presto, C. Artini, M. Pani, M.M. Carnaciali, S. Massardo, M. Viviani, Ionic conductivity and local structure features in $Ce_{1-x}Sm_xO_{2-x/2}$, J. Phys. Chem. Phys. 20 (2018) 28338-28345.

(34) J.D. Wang, Y.H. Xie, Z.F. Zhang, R.Q. Liu, Z.J. Li, Protonic conduction in Ca^{2+}-doped $La_2M_2O_7$ (M=Ce, Zr) with its application to ammonia synthesis electrochemically. Mater. Res. Bull. 40 (2005) 1294-1302.

(35) Y. Wu, Z. Gong, J. Hou, L. Miao, H. Tang, Liu, Wei. An easily sintered and chemically stable $La_{2-x}Mg_xCe_2O_{7-\delta}$ proton conductor for high-performance solid oxide fuel cells. Int. J. Hydrog. Energy, 44 (2019) 13835-13842.

(36) T. Tu, J. Liu, K. Peng, Preparation and performance of Na-doped $La_2Ce_2O_7$ electrolytes for protonic ceramic fuel cells. Ceram. Int. 43 (2017) 16384-16390.

(37) H.-S. Zhang, J.-G. Lv, G. Li, X.-G. Chen, X.-L. Wang, Preparation, characterization, and thermophysical properties of $(La_{0.95}Sr_{0.05})_2Ce_2O_{6.95}$ ceramic for thermal barrier coatings. Int. J. Appl. Ceram. Tec. 11 (2014) 350-358.

(38) J. Xu, Y. Zhang, Y. Liu, X. Fang, X. Xu, W. Liu, R. Zheng, X. Wang, Optimizing the Reaction Performance of $La_2Ce_2O_7$-Based Catalysts for Oxidative Coupling of Methane (OCM) at Lower Temperature by Lattice Doping with Ca Cations. Eur. J. Inorg. Chem. 2 (2019) 183-194.

(39) L. Yan, W. Sun, L. Bi, S. Fang, Z. Tao, W. Liu, Effect of Sm-doping on the hydrogen permeation of Ni–$La_2Ce_2O_7$ mixed protonic–electronic conductor. Int. J. Hydrog. Energy, 35 (2010) 4508-4511.

(40) T. Tu, B. Zhang, J. Liu, K. Wu, K. Peng, Synthesis and conductivity behaviour of Mo-doped $La_2Ce_2O_7$ proton conductors. Electrochim. Acta 283 (2018) 1366-1374.

(41) H. Zhang, J. Sun, S. Duo, X. Zhou, J. Yuan, S. Dong, X, Yang, J. Zeng, J. Jiang, L. Deng, X. Cao, Thermal and mechanical properties of Ta_2O_5 doped $La_2Ce_2O_7$ thermal barrier coatings prepared by atmospheric plasma spraying. J. Eur. Ceram. Soc. 39 (2019) 2379-2388.

(42) B. Zhang, Z. Zhong, T. Tu, K. Wu, K. Peng, Acceptor-doped $La_{1.9}M_{0.1}Ce_2O_7$ (M = Nd, Sm, Dy, Y, In) proton ceramics and in-situ formed electron-blocking layer for solid oxide fuel cells applications. J. Power Sources 412 (2019) 631-639.

(43) H. Wang, R. Peng, X. Wu, J. Hu, C. Xia, Sintering Behavior and Conductivity Study of yttrium-doped $BaCeO_3$–$BaZrO_3$ solid solutions using ZnO additives. J. Am. Ceram. Soc. 92 (2009) 2623-2629.

(44) PANalytical X´Pert HighScore Plus suite, B.V., Lelyweg 1, 7602 EA Almelo, The Netherlands, 2014.

(45) A.C. Larson, R.B. von Dreele, General Structure Analysis System (GSAS), Los Alamos National Lab, 1994.

(46) I. Kosacki, V. Petrovsky, H. U. Anderson, P. Colomban, Raman Spectroscopy of Nanocrystalline Ceria and Zirconia Thin Films J. Am. Ceram. Soc., 85 (2002) 2646–2650.

(47) B.P. Mandal, V. Grover, M. Roy, A.K. Tyagi, X-Ray Diffraction and Raman Spectroscopic Investigation on the Phase Relations in Yb_2O_3- and Tm_2O_3-Substituted CeO_2. J. Am. Ceram. Soc. 90 (2007) 2961–2965.

(48) A. Nakajima, A. Yoshihara, M. Ishigame, Defect-induced Raman spectra in doped CeO_2-Gd_2O_3 solid solutions. Phys. Rev. B: Condens. Matter Mater. Phys. 50 (1994) 13297-13307.

(49) S. Escolástico, C. Solís, T. Scherb, G. Schumacher, J.M. Serra, Hydrogen separation in $La_{5.5}WO_{11.25-\delta}$ membranes. J. Membrane Sci. 444 (2013) 276-284.

(50) J.T.S. Irvine, D.C. Sinclair, A.R. West, Electroceramics: characterization by impedance spectroscopy. Adv. Mater. 2 (1990) 132-138.

(51) W. Ma, S. Gong, H. Xu, X. Cao. On improving the phase stability and thermal expansion coefficients of lanthanum cerium oxide solid solutions. Scripta Mater. 54 (2006) 1505-1508.

(52) S. Yamanaka, M. Fujikane, T. Hamaguchi, H. Muta, T. Oyama, T. Matsuda, S. Kobayashi, K. Kurosaki. Thermophysical properties of $BaZrO_3$ and $BaCeO_3$. J. Alloy Compd. 359 (2003) 109-113.

(53) A. Maheshwari, H.-D. Wiemhöfer, Optimized mixed ionic–electronic conductivity in two-phase ceria–zirconia composite with cobalt oxide and Na_2CO_3 as suitable additives, J. Mater. Chem. A 4 (2016) 4402-4412.

(54) H. Yamamura, H. Nishino, K. Kakinuma, K. Nomura, Crystal Phase and Electrical Conductivity in the Pyrochlore-Type Composition Systems, $Ln_2Ce_2O_7$ (Ln = La, Nd, Sm, Eu, Gd, Y and Yb). J. Ceram. Soc. Jpn. 111, (2003) 902-906.

(55) M. Amsif, D. Marrero-López, A. Magrasó, J. Peña-Martínez, J.C. Ruíz-Morales, P. Núñez, Synthesis and characterisation of $BaCeO_3$-based proton conductors obtained from freeze-drying precursors. J. Eur. Ceram. Soc. 29 (2009) 131-138.

(56) G.S. Reddy, R. Baury, Y and In-doped $BaCeO_3$-$BaZrO_3$ solid solutions: Chemically stable and easily sinterable proton conducting oxides. J. Alloy Compd. 688 (2016) 1039-1046.

(57) J. P.F. Grilo, D. A. Macedo, R. M. Nascimento, F. M.B. Marques, Electronic conductivity in Gd-doped ceria with salt additions, Electrochim Acta 318 (2019) 977-988.

Figure 1.

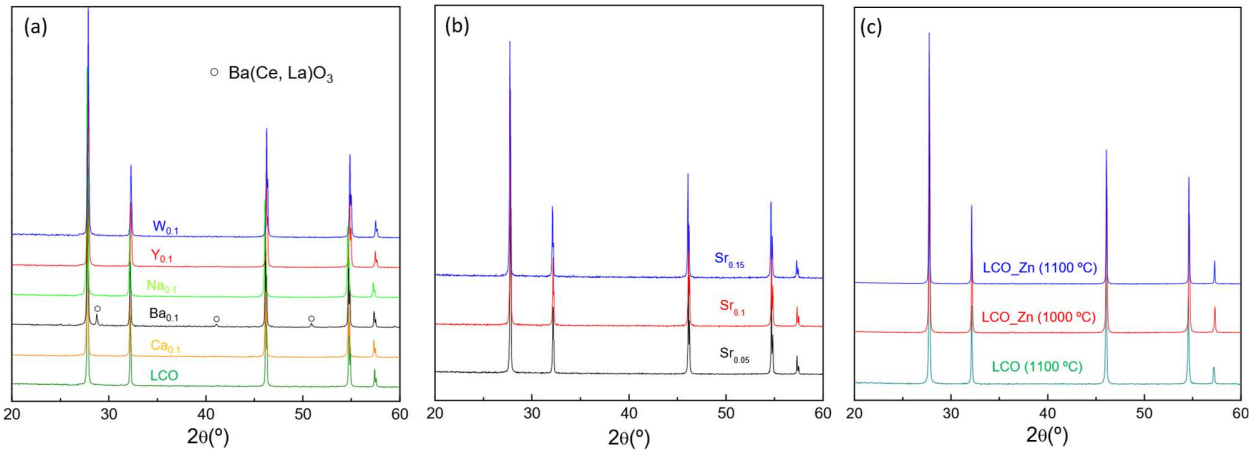
(a)
○ Ba(Ce, La)O3
W0.1
Y0.1
Na0.1
Ba0.1
Ca0.1
LCO
20
30
40
50
60
2θ(°)
(b)
Sr0.15
Sr0.1
Sr0.05
20
30
40
50
60
2θ(°)
(c)
LCO_Zn (1100 °C)
LCO_Zn (1000 °C)
LCO (1100 °C)
20
30
40
50
60
2θ(°)

Figure 2.

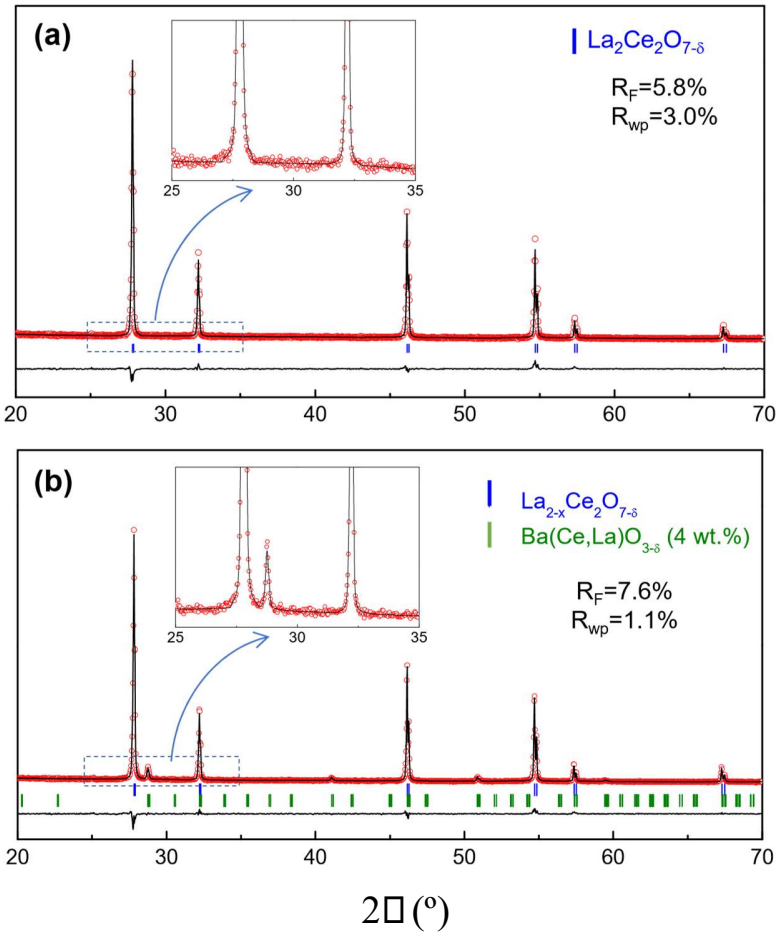

Figure 3.

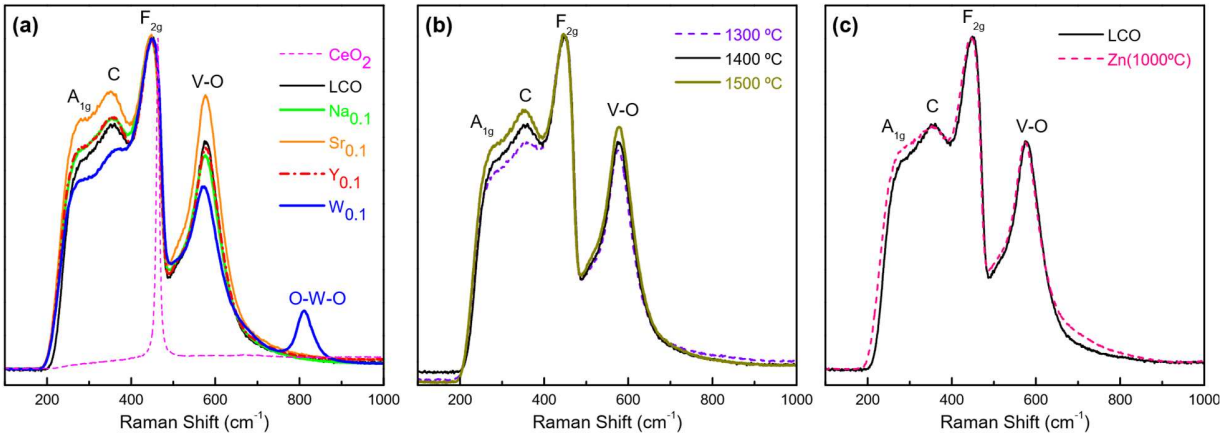

Figure 4.

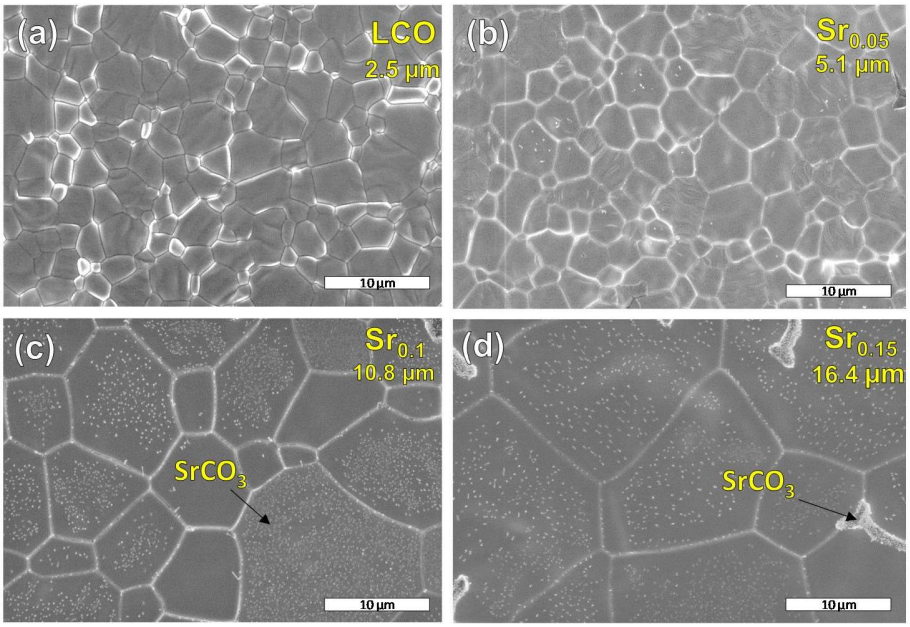
(a)
LCO
2.5 µm
10 µm
(b)
Sr0.05
5.1 µm
10 µm
(c)
Sr0.1
10.8 µm
SrCO3
10 µm
(d)
Sr0.15
16.4 µm
SrCO3
10 µm

Figure 5.

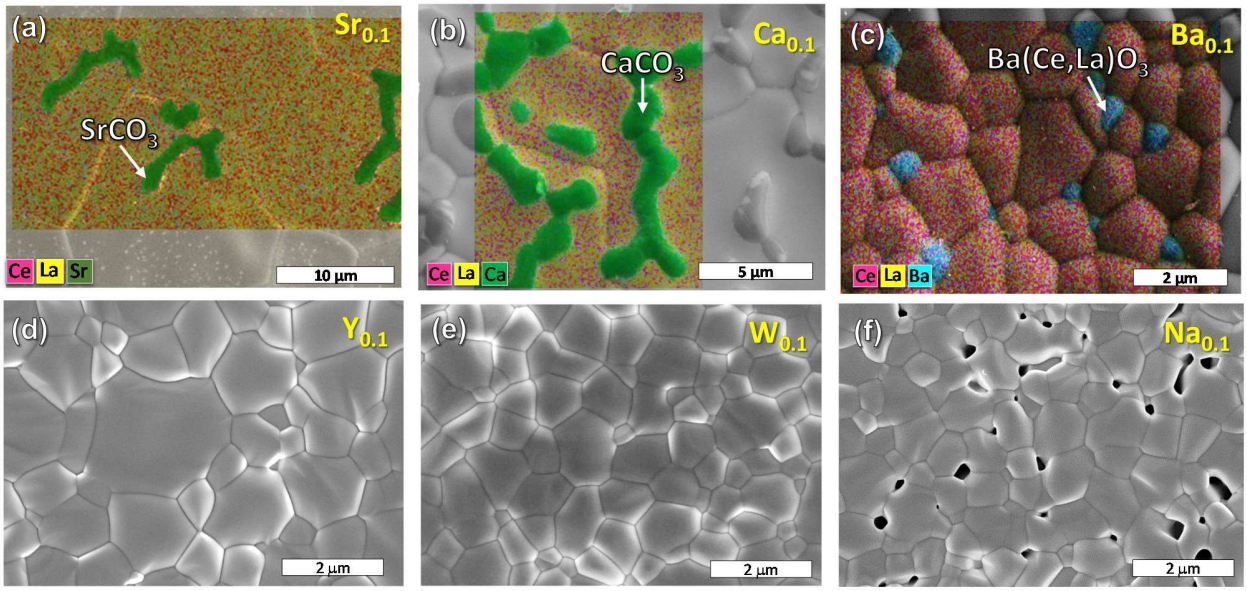
(a)
Sr0.1
SrCO3
Ce La Sr
10 µm
(b)
Ca0.1
CaCO3
Ce La Ca
5 µm
(c)
Ba0.1
Ba(Ce,La)O3
Ce La Ba
2 µm
(d)
Y0.1
2 µm
(e)
W0.1
2 µm
(f)
Na0.1
2 µm

Figure 6.

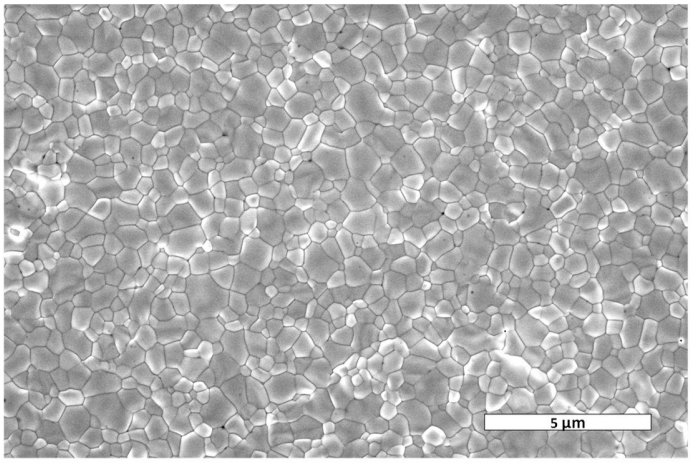

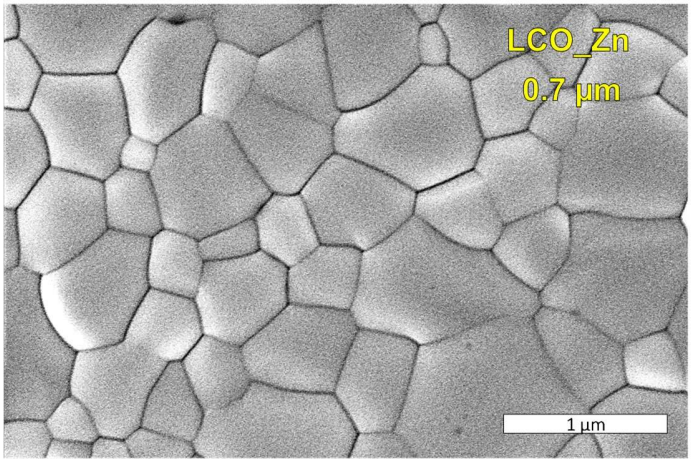

Figure 7.

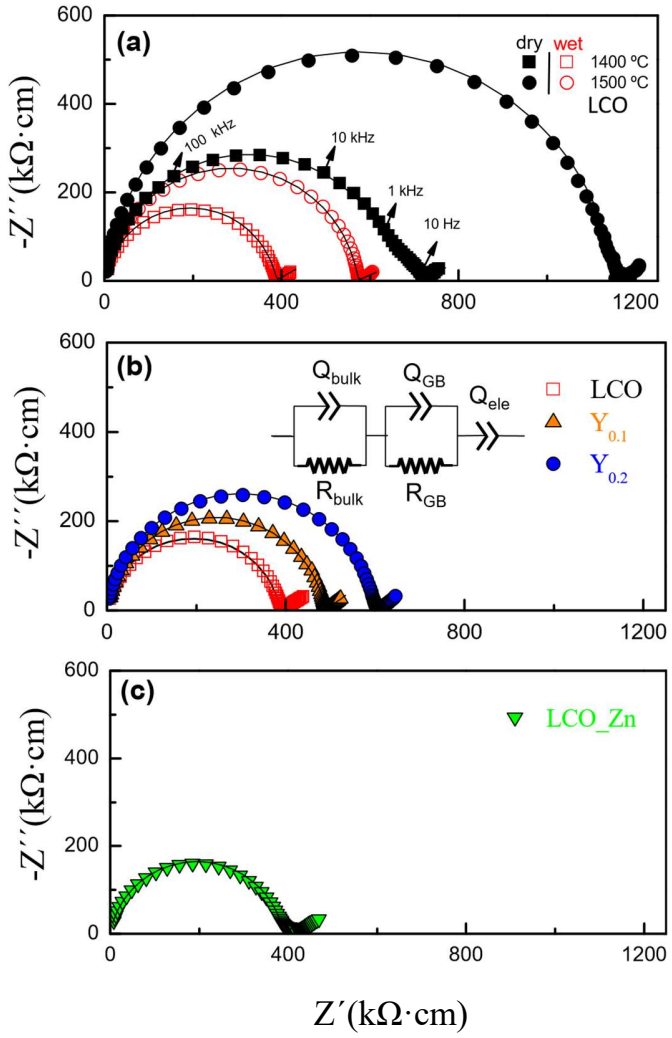
(a)
dry wet
1400 °C
1500 °C
LCO
100 kHz
10 kHz
1 kHz
10 Hz
-Z′′(kΩ·cm)
(b)
Q_bulk
Q_GB
Q_ele
R_bulk
R_GB
LCO
Y0.1
Y0.2
(c)
LCO_Zn
Z′(kΩ·cm)

Figure 8.

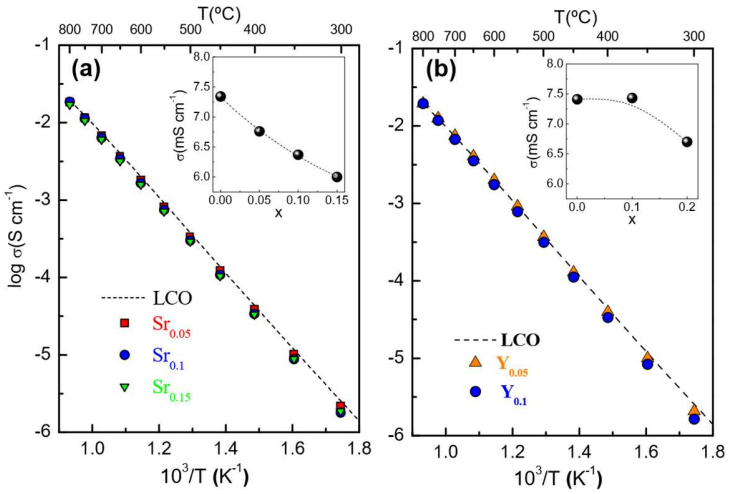
T(°C)
(a)
log σ(S cm⁻¹)
σ(mS cm⁻¹)
x
LCO
Sr0.05
Sr0.1
Sr0.15
10³/T (K⁻¹)
(b)
LCO
Y0.05
Y0.1

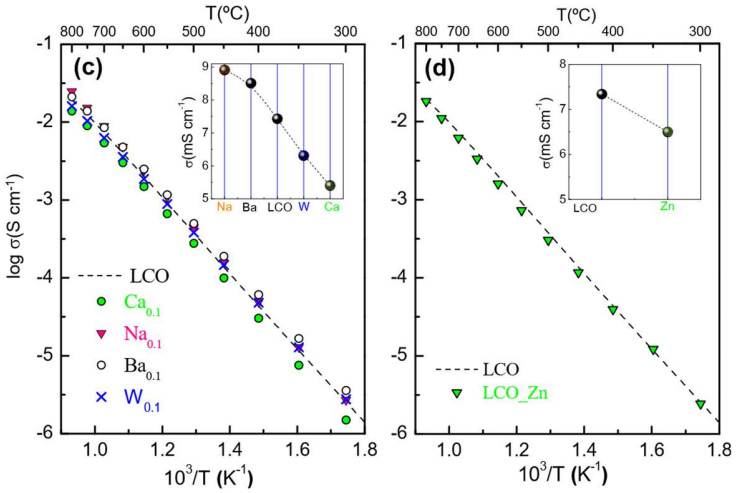
T(ºC)
800 700 600 500 400 300
(c)
log σ(S cm-1)
LCO
Ca0.1
Na0.1
Ba0.1
W0.1
10^3/T (K^-1)
σ(mS cm-1)
Na Ba LCO W Ca
(d)
LCO
LCO_Zn
LCO Zn